Thermal conductivity of math xmlns="http://www.w3.org/1998/Math/MathML">msub>mi >CaSiO/mi>mn>3/mn>/msub>/math> perovskite at lower mantle conditions

Zhen Zhang, Dong-Bo Zhang, Kotaro Onga, Akira Hasegawa, Kenji Ohta, Kei Hirose, and Renata M. Wentzcovitch

Phys. Rev. B **104**, 184101 — Published 4 November 2021

DOI: 10.1103/PhysRevB.104.184101

Thermal Conductivity of $CaSiO_3$ Perovskite at Lower Mantle Conditions

Zhen Zhang[1], Dong-Bo Zhang[2,3], Kotaro Onga[4], Akira Hasegawa[4,5], Kenji Ohta[4], Kei Hirose[6,7], and Renata M. Wentzcovitch[1,8,9,*]

[1]*Department of Applied Physics and Applied Mathematics, Columbia University, New York, NY 10027, USA.*

[2]*College of Nuclear Science and Technology, Beijing Normal University, Beijing 100875, People's Republic of China.*

[3]*Beijing Computational Science Research Center, Beijing 100193, People's Republic of China.*

[4]*Department of Earth and Planetary Sciences, Tokyo Institute of Technology, Meguro, Tokyo 152-8551, Japan.*

[5]*National Metrology Institute of Japan, National Institute of Advanced Industrial Science and Technology, Tsukuba, Ibaraki 305-8563, Japan.*

[6]*Department of Earth and Planetary Science, The University of Tokyo, Bunkyo, Tokyo 113-0033, Japan.*

[7]*Earth-Life Science Institute, Tokyo Institute of Technology, Meguro, Tokyo 152-8550, Japan.*

[8]*Department of Earth and Environmental Sciences, Columbia University, New York, NY 10027, USA.*

[9]*Lamont–Doherty Earth Observatory, Columbia University, Palisades, NY 10964, USA.*

[*]To whom correspondence should be addressed.

rmw2150@columbia.edu

Abstract

Thermal conductivity (κ) of mantle minerals is key to understanding dynamics in the deep Earth. It controls the style of mantle convection and the time scale of cooling both the mantle and the core. Cubic $CaSiO_3$ perovskite (CaPv) is the third most abundant mineral in the lower mantle (7 vol%). Despite its importance, no theoretical nor experimental estimate of CaPv's κ is available. Theoretical investigations of its properties are challenging because of its strong anharmonicity. Experimental measurements at relevant pressures and temperatures are equally challenging. Here we present *ab initio* results for CaPv's κ obtained using the phonon quasiparticle approach to address its strong anharmonicity. We also offer experimental measurements of κ up to 67 GPa and 1950 K. Predictions and measurements are in good agreement and reveal a surprisingly large κ for cubic CaPv that can be explained on the basis of its high crystal structure symmetry. Despite its relatively low abundance, CaPv's κ increases the lower mantle κ by ~10%, if accounted for. κ of mantle regions enriched in subducted crustal materials will be more strongly impacted.

I. INTRODUCTION

The dominant mode of heat transport between the Earth's core and the surface controls the planet's internal dynamics and evolution. The core-mantle boundary (CMB) located at 2890 km depth is the interface between the molten metallic core and the rocky mantle. At the CMB, where mass transport is impeded, the lower mantle (LM) receives heat from the core via conduction [1]. Knowledge of κ of LM minerals is critical for constraining predictions of the CMB heat flow [2], which provides a basis for understanding the Earth's dynamic state and thermal history and the relative importance of conduction versus convection above the CMB. The LM extends from 670 to 2890 km in depth, constituting 55 vol% of the Earth's whole interior. Pressures (P) and temperatures (T) in this region vary between $23 < P < 135$ GPa and $2000 < T < 4000$ K [3,4]. Such conditions introduce considerable challenges for both measurements and theoretical estimates of thermal conductivity of mantle minerals, precluding precise constraints of LM's κ [2,5,6]. Thus, the understanding of thermal conduction through the LM is still incomplete [1].

$CaSiO_3$ perovskite (CaPv) constitutes ~7 vol% of a pyrolitic LM [7,8]. Despite its importance, no previous estimate of cubic CaPv's lattice thermal conductivity, κ_{lat}, is available owing to its strong anharmonicity, i.e., strong phonon-phonon interactions. Anharmonicity manifests as an intrinsic temperature dependence in phonon frequencies at constant volume [9,10]. CaPv assumes a cubic structure [9,11,12] under LM conditions, but it is dynamically unstable below 500 K [9,13]. At low temperatures, it presents tetragonal and orthorhombic distortions [14]. Measurements of cubic CaPv's κ_{lat} need to be carried out above ~600 K and ~26 GPa [9,11]. It is indispensable to determine the κ_{lat} of cubic CaPv *in-situ* at high *P-T* because this phase is unquenchable. Calculations of κ_{lat} are also challenging. Prevailing *ab initio* approaches relying on perturbative treatments of weak anharmonicity up to three-phonon scattering processes have been used to evaluate κ_{lat} of MgO periclase (Pc) [15-17], pure bridgmanite, i.e., $MgSiO_3$ perovskite (MgPv) [18-20], and $MgSiO_3$ postperovskite (MgPPv) [21], the second and first most abundant phases of the LM, and the most abundant phase of the D" region, respectively. However, these approaches are invalid for cubic CaPv since static density-functional theory (DFT) calculations of cubic CaPv yield a double-well potential [9,22] that renders the cubic phase unstable at low temperatures. The deviation from harmonic potential is substantial, and thus, the harmonic phonon calculations acquire imaginary frequencies [9,22]. Only at sufficiently high temperatures, the cubic phase is

dynamically stabilized by anharmonic interactions, and the phonon dispersion is free of imaginary frequencies [9].

Here, we investigate the *P-T* dependence of cubic CaPv's κ_{lat} using *ab initio* calculations and direct measurements. We use the phonon quasiparticle approach [10,23] that can address the strongly anharmonic nature of CaPv, and pulsed light heating thermoreflectance to measure κ_{lat} in a laser-heated diamond anvil cell (DAC) (see Appendix) [24,25]. Calculations and experiments reveal anomalously high κ_{lat} for CaPv. We use these results and similar ones on MgPv and Pc to estimate κ_{lat} of a pyrolitic aggregate at LM conditions.

II. METHOD

Heat transport in pure crystalline insulators is governed by phonon-phonon scatterings. Lattice thermal conductivity can be calculated with the relaxation-time approximation (RTA) of the linearized Boltzmann transport equation (LBTE) [26,27] when phonon quasiparticles exist,

$$\kappa_{lat} = \frac{1}{3}\sum_{\mathbf{q}s} c_{\mathbf{q}s} v_{\mathbf{q}s} l_{\mathbf{q}s}, \quad (1)$$

where $c_{\mathbf{q}s}$, $v_{\mathbf{q}s}$, $l_{\mathbf{q}s} = v_{\mathbf{q}s}\tau_{\mathbf{q}s}$ and $\tau_{\mathbf{q}s}$ are phonon heat capacity, group velocity, mean free path, and lifetime, respectively, of normal mode ($\mathbf{q}$, s) with frequency $\omega_{\mathbf{q}s}$. $\mathbf{q}$ is the phonon wave vector, and s runs over the 3n phonon branches of an n-atom primitive cell. Under high temperatures ($T \geq$ 1300 K) investigated here, $c_{\mathbf{q}s}$ is simply $k_{\mathbf{B}}$ in the classical limit. The RTA usually works well at high temperatures and is found to give <1% difference in κ_{lat} compared with the iteratively solved full solution to the LBTE for MgPv [20]. The isotope scattering, which is found to give an insignificant reduction in κ_{lat} for MgPv (1–3% [20]) and Pc (4% [15]), also diminishes at high temperatures and is disregarded in this study. Thus, $v_{\mathbf{q}s}$ and $\tau_{\mathbf{q}s}$ are the critical quantities needed to evaluate κ_{lat}. For weakly anharmonic systems, $v_{\mathbf{q}s}$ and $\tau_{\mathbf{q}s}$ are routinely [28,29] determined using density-functional perturbation theory (DFPT) and many-body perturbation theory. However, conventional perturbative treatments relying on the finite displacement method to calculate anharmonic phonon properties without renormalization of force constants become invalid in the presence of strong anharmonicity. There are several methods implementing the force renormalization beyond the conventional perturbative approaches, either through a self-consistent iterative scheme [30-33] or from *ab initio* MD [34,35]. They have been used to study both weakly [31,32,34] and strongly [31,33,35] anharmonic solids. Nevertheless, they have not been widely

applied to strongly anharmonic crystals with imaginary frequencies such as CaPv. Here we tackle this strongly anharmonic problem using the phonon quasiparticle method [10,23]. The latter has successfully addressed various problems caused by strong anharmonicity [9,36], notably the stabilization of CaPv's cubic phase above ~600 K at ~26 GPa [9], the *hcp* to *bcc* phase transition of metallic beryllium [36,37], and the phase stabilities and thermal conductivities of PbTe and SnSe [38-40]. In this approach, phonon anharmonicity is expressed in terms of two quantities; renormalized phonon frequencies, $\widetilde{\omega}_{\mathbf{q}s}$, and lifetimes, $\tau_{\mathbf{q}s}$. These quantities and the phonon group velocity, $v_{\mathbf{q}s} = d\widetilde{\omega}_{\mathbf{q}s}/d\mathbf{q}$, are all temperature-dependent.

Phonon quasiparticle properties are obtained by computing the mode-projected velocity autocorrelation function (VAF) [9,10],

$$\langle V_{\mathbf{q}s}(0) \cdot V_{\mathbf{q}s}(t) \rangle = \lim_{\tau\to\infty} \frac{1}{\tau} \int_0^\tau V_{\mathbf{q}s}^*(t') V_{\mathbf{q}s}(t'+t) dt', \quad (2)$$

where $V_{\mathbf{q}s}(t) = \sum_{i=1}^{N} \sqrt{M_i} \mathbf{v}_i(\mathrm{t}) e^{i\mathbf{q}\cdot\mathbf{R}_i} \cdot \hat{\mathbf{e}}_{\mathbf{q}s}$ is the mass-weighted and (**q**, *s*)-mode-projected velocity. $\mathbf{v}_i(t)(i = 1, \ldots, N)$ are the atomic velocities obtained from MD trajectories of an *N*-atom supercell. M_i and $\mathbf{R}_i$ are the atomic mass and the atomic equilibrium coordinate of the i^{th} atom in the supercell, respectively. $\hat{\mathbf{e}}_{\mathbf{q}s}$ is the polarization vector of the harmonic phonon for mode (**q**, *s*), and **q** is commensurate with the supercell size. The power spectrum of a well-defined phonon quasiparticle, $G_{\mathbf{q}s}(\omega) = \left| \int_0^\infty \langle V_{\mathbf{q}s}(0) \cdot V_{\mathbf{q}s}(t) \rangle e^{i\omega t} dt \right|^2$ has a Lorentzian line shape with a single peak at $\widetilde{\omega}_{\mathbf{q}s}$ and a linewidth of $\Gamma_{\mathbf{q}s} = 1/(2\tau_{\mathbf{q}s})$. In principle, a complete decay of the VAF is required to obtain a reliable $G_{\mathbf{q}s}$. However, very long MD runs are required to meet this condition for phonon quasiparticles with long lifetimes, which is inconvenient for *ab initio* MD simulations. Here we extract $\widetilde{\omega}_{\mathbf{q}s}$ and $\tau_{\mathbf{q}s}$ from the VAF from relatively shorter MD simulations. For a well-defined quasiparticle of mode (**q**, *s*), one can simply fit the VAF phenomenologically to the expression [23],

$$\langle V_{\mathbf{q}s}(0) \cdot V_{\mathbf{q}s}(t) \rangle = A_{\mathbf{q}s} \cos(\widetilde{\omega}_{\mathbf{q}s} t) e^{-\Gamma_{\mathbf{q}s} t}, \quad (3)$$

where $A_{\mathbf{q}s}$ is the oscillation amplitude. Here for cubic CaPv in the relevant temperature range, all the phonon quasiparticles sampled by the MD simulations are well-defined, the VAF of which can be perfectly described by Eq. (3). In practice, for well-defined VAF, to obtain reliable $\widetilde{\omega}_{\mathbf{q}s}$ and $\tau_{\mathbf{q}s}$, the fitting needs only the numerical data of $\langle V_{\mathbf{q}s}(0) \cdot V_{\mathbf{q}s}(t) \rangle$ for the first few oscillation periods [10,41], e.g., till the oscillation amplitude decays to its half maximum. $\widetilde{\omega}_{\mathbf{q}s}$, $\tau_{\mathbf{q}s}$ and $A_{\mathbf{q}s}$ are

obtained simultaneously by the least square fitting. Figure S1 of the Supplemental Material [42] showcases the VAF of a phonon mode for CaPv at 2000 K and the corresponding fitting curve. The changes in $\widetilde{\omega}_{\mathbf{q}s}$ and $\tau_{\mathbf{q}s}$ by conducting the fitting for several more or fewer oscillation periods of the VAF are negligible, indicating the convergence of quasiparticle properties.

We carried out *ab initio* MD simulations in the *NVT* ensemble and phonon calculations with the DFT-based Vienna *ab initio* simulation package (VASP) [28] employing the local density approximation (LDA) and the projected-augmented wave method (PAW) [68]. The kinetic energy cutoff adopted was 550 eV. MD simulations were conducted on $2 \times 2 \times 2$ (40 atoms) and $3 \times 3 \times 3$ supercells (135 atoms) for a series of volumes (44.39, 40.26, 36.77, 34.34 and 32.49 Å^3/primitive cell) corresponding to densities 4.35, 4.79, 5.25, 5.62, and 5.94 g/cm^3, respectively. A previous study [9] has shown that $2 \times 2 \times 2$ supercells (40 atoms) are sufficient to converge the anharmonic interactions and anharmonic phonon dispersions. In this study, we used the $3 \times 3 \times 3$ **q**-mesh to investigate the behavior of phonon lifetimes. We carried out isochoric MD simulations for temperatures ranging from 1300 to 4000 K controlled by the Nosé thermostat [69] for over 60 ps with a time step of 1 fs. Throughout the volume and temperature range considered, the cubic CaPv phase was confirmed to be stable, and phonon quasiparticles were well-defined. Harmonic phonon frequencies and normal modes were calculated using DFPT [70] implemented in the VASP package. Anharmonic phonon dispersions and phonon lifetimes were extracted from the phonon quasiparticles sampled by the MD simulations [9,41]. Similar MD simulations were also conducted for MgO periclase (Pc) with $4 \times 4 \times 4$ supercells (128 atoms) and *Pbnm* $MgSiO_3$ perovskite (MgPv) with $2 \times 2 \times 2$ supercells (160 atoms). Since the focus of this paper is on CaPv, we report only a few results on these systems here.

III. RESULTS AND DISCUSSION

Ab initio simulations combining lattice dynamics and molecular dynamics (MD) give phonon quasiparticle properties of cubic CaPv at LM conditions. Figure 1 shows $v_{\mathbf{q}s}$ and $\tau_{\mathbf{q}s}$ versus $\widetilde{\omega}_{\mathbf{q}s}$ collected in 135-atom MD simulations at various temperatures for ρ = 4.79 g/cm^3. $\widetilde{\omega}_{\mathbf{q}s}$ and $v_{\mathbf{q}s}$ show a mild and nonmonotonic temperature dependence (Fig. 1(a)), while the temperature dependence is relatively stronger for $\tau_{\mathbf{q}s}$ (Fig. 1(b)). Sub-minimal mean free paths [43], $l_{\mathbf{q}s}$, are observed for CaPv and are shown in Fig. S2 of the Supplemental Material [42].

To obtain κ_{lat} converged in the thermodynamic limit, the summation in Eq. (1) must be carried out over a dense **q**-mesh throughout the Brillouin zone (BZ). The number of **q**-vectors sampled in MD simulations is limited by the supercell size. Therefore, it is desirable to find a parameterization of $\tau_{\mathbf{q}s}$'s dependence on frequency [43,47,71,72]. We rely on such parametrization [42] to obtain $\tau_{\mathbf{q}s}$ on a dense, converged **q**-mesh. The parameterized values of $\tau_{\mathbf{q}s}$ at 1300 K are shown in Fig. 2(a). Anharmonic phonon dispersion is obtained by Fourier interpolation [9,10], and $v_{\mathbf{q}s}$ can be calculated on any desired **q**-mesh, as also shown in Fig. 2(a). For comparison, we show $\tau_{\mathbf{q}s}$ and $v_{\mathbf{q}s}$ of MgPv [42,43] in Fig. 2(b).

We have also computed the average lifetimes, $\bar{\tau}$, and average velocities, $\bar{v}$. Figures 2(c) and 2(d) show their pressure and temperature dependence for CaPv and MgPv. Despite being strongly anharmonic, CaPv's $\bar{\tau}$ and $\bar{v}$ are larger than those of MgPv at all temperatures and pressures considered. Such behavior is unexpected because MgPv is weakly anharmonic [10,20,43] and less dense than CaPv. Note that only acoustic branches of CaPv in the narrow region of the BZ marked by the dashed rectangle in Fig. 2(e) show strong temperature dependence. Compared with the phonon dispersion of MgPv shown in Fig. 2(f), the temperature dependence of the optical modes in CaPv and MgPv are similar. Plotting these phonon dispersions in their respective BZ's highlights another essential fact. Cubic ($Pm\bar{3}m$, 5 atoms/cell) CaPv has higher symmetry and fewer reflections at BZ edges than orthorhombic ($Pbnm$, 20 atoms/cell) MgPv. MgPv's phonon branches are folded into a smaller BZ and show less dispersive optical branches with lower velocities. Branch folding in some cases causes repulsive branch interaction that reduces $v_{\mathbf{q}s}$. These branch folding effects are quite visible when comparing phonon velocities in Figs. 2(a) and 2(b). Above ~250 cm^{-1}, CaPv's $v_{\mathbf{q}s}$ are generally larger than those of MgPv. More importantly, the proportion of acoustic branches with high $v_{\mathbf{q}s}$ and long $\tau_{\mathbf{q}s}$ for CaPv (3/15) is much larger than that for MgPv (3/60). Therefore, CaPv's higher crystal structure symmetry leads to higher $\bar{v}$ and larger κ_{lat}.

Employing these $v_{\mathbf{q}s}$ and $\tau_{\mathbf{q}s}$ computed in the thermodynamic limit, we have calculated κ_{lat} of CaPv at several densities (ρ) and temperatures using Eq. (1) (Fig. 3(a)). The density and temperature effects on κ_{lat} can be described by [48,73]

$$\kappa_{lat} = \kappa_{ref}\left(\frac{T_{ref}}{T}\right)^{a}\left(\frac{\rho}{\rho_{ref}}\right)^{g}, \quad (4)$$

where g is $g = b\, ln\left(\frac{\rho}{\rho_{ref}}\right) + c$ [73]. By choosing the reference density (ρ_{ref}) as 4.35 g/cm^3 and reference temperature (T_{ref}) as 1300 K, we obtained the fitting parameters κ_{ref}, a, b and c as 10.9 W/m/K, 1.11, -10.2 and 7.87, respectively (solid curves in Fig. 3(a)). The choice of ρ_{ref} and T_{ref} is not unique, but they do not change the density and temperature dependence of κ_{lat}. At each density, κ_{lat} varies approximately as $1/T^{1.11}$, i.e., it decays faster than the theoretically expected $1/T$ relation. The $1/T$ dependence is associated with the dominant three-phonon scattering processes. With increasing temperature, four-phonon and higher-order phonon scatterings become important, enabling more phonon decay channels. Hence, κ_{lat} is expected to decay faster than $1/T$ at high temperatures [74]. However, such dependence only applies within the temperature range investigated in this study, where the cubic phase is adopted, and phonon quasiparticles are well-defined.

$\kappa_{lat}(T, \rho)$ are converted into $\kappa_{lat}(T, P)$ by using an accurate thermal equation of state of cubic CaPv [75], which was developed by carefully combining [76,77] anharmonic free energy, $F(T,V)$, and pressure, $P(T,V)$ [10,36], with experimental data [12,78]. Converted results for $\kappa_{lat}(T, P)$ are shown in Fig. 3(b). There are two notable features in $\kappa_{lat}(T, P)$'s behavior. First, κ_{lat} is considerably large against the conventional wisdom that strong anharmonicity reduces thermal conductivity. At the onset of the D" region at 2600 km depth (T = 2735 K and P = 120 GPa), κ_{lat} = 16.3(10) W/m/K, which is about 2.5 times as great as that of MgPv (6.5(4) W/m/K [42]). This relationship applies approximately to the entire LM. This relatively large κ_{lat} of CaPv results mainly from CaPv's high crystal structure symmetry (see discussion above). Second, κ_{lat} varies linearly with pressure, similarly to MgPv [6] and Pc [56] observed by experiments. This feature has also been reproduced by *ab initio* studies of MgPv [20,43] and Pc [79].

Such counterintuitive results call for experimental validation. To obtain CaPv's κ_{lat}, a combination of pulsed light heating thermoreflectance and laser-heated DAC techniques was employed for the measurements of thermal diffusivity *in-situ* at high *P-T* conditions (see Appendix) [24,25]. The measured values for CaPv are summarized in TABLE I and shown in Fig. 3(b). Four separate measurements were performed at ~1300 K, and one at 1950 K. The measured κ_{lat} compare well with the calculated values within experimental and computational uncertainties. Such an agreement further validates the present theoretical approach.

There are reports of strongly anharmonic perovskites with ultralow κ_{lat} [35,80]. Such systems are quite different from CaPv, the leading cause of the distinct κ_{lat} being CaPv's much larger phonon velocities originating in the wider frequency range of phonon dispersions (>1000 cm^{-1} for CaPv and <170 cm^{-1} in [35,80]). Besides, many of the ultralow-κ_{lat} systems were investigated near their 2nd-order phase transition temperature range [35,80], in which the single-phonon power spectrum exhibits strong broadening and non-Lorentzian features. In such a case, the validity of phonon quasiparticles and the applicability of the LBTE are debatable. In these ultralow-κ_{lat} materials, the small frequency range also leads to closely spaced phonon branches, and thus, strong coupling between different phonon eigenstates. Whether the off-diagonal wavelike tunneling terms of the heat flux operator contribute significantly to the thermal conductivity may need to be studied as well [33,80,81]. The 2nd-order phase transition for CaPv happens below ~600 K at ~26 GPa [9], through which the single-phonon power spectrum exhibits strong non-Lorentzian features with double peaks [9]. The corresponding phonon lifetime should be very short. The present study focuses on $T \geq 1300$ K, which is well above CaPv's 2nd-order phase transition temperatures for the LM pressures. All the phonon quasiparticles are well-defined, corresponding Lorentzian power spectra allow extraction of well-defined lifetimes, phonon branches are sparsely spaced, and the RTA of the LBTE is applicable.

The recently reported values of κ_{lat} and total thermal conductivity (κ_{tot}) of the LM, the latter including a radiative contribution (κ_{rad}), considered the LM as a mixture of MgPv and Pc only [18,19,48,49,51,52]. In the LM, both MgPv and Pc contain significant amounts of iron, and MgPv also contains aluminum; therefore, it is necessary to consider the impact of these substitutions on κ_{lat}. Such an impact was shown to be substantial, reducing κ_{lat} by ~50% for MgPv and Pc [48]. By including the impurity effects and the radiative contribution [2,19], theoretical and experimental estimations of κ_{lat} [48-52] and κ_{tot} [18,19] of the LM has yielded large uncertainties (Fig. 4). However, the contribution of CaPv has been omitted [18,19,48,49,51,52] in these studies.

With a large κ_{lat}, CaPv should contribute significantly to the κ_{lat} of the LM. CaPv contains insignificant amounts of iron and aluminum and their effect on κ_{lat} should be negligible. Therefore, it is reasonable to approximate the *ab initio* value of CaPv's κ_{lat} as its LM value. Our predicted κ_{lat} along a typical LM geotherm [60] with a thermal boundary layer above the CMB is shown in Fig. 4. We compute κ_{tot} of the LM in the following four steps. First, κ_{lat} of pure MgPv

and pure Pc were also investigated [42] using the same method. The obtained κ_{lat} are shown in Figs. S3 and S4 of the Supplemental Material [42], respectively. Second, as in previous studies, we assume κ_{lat} values of MgPv and Pc are reduced by 50% after considering impurity effects [48]. Third, κ_{lat} of a pyrolitic LM, i.e., ~7 vol% CaPv, ~75 vol% bridgmanite (postperovskite in the D" region [21]), and ~18 vol% ferropericlase [7], is obtained using the Voigt-Reuss-Hill averaging [49,66] scheme. Fourth, κ_{tot} is obtained by adding the recent experimental determination of κ_{rad} of a pyrolitic aggregate [53] to κ_{lat}. κ_{tot} of the LM along the geotherm is shown in Fig. 4, along with several other previous estimates [18,19,48-52]. We predict κ_{tot} = 6.0(4) W/m/K at 2600 km depth, and κ_{tot} = 4.9(3) W/m/K at the CMB. The Supplemental Material [42] presents a discussion on discrepancies between different published results. With its relatively low abundance (~7 vol%), the inclusion of CaPv increases κ_{lat} of the LM by ~11% and κ_{tot} by ~9% at all depths. In regions populated with subducted mid-ocean ridge basalt (MORB) [13], where CaPv is more abundant (>23 vol% [61]), the inclusion of CaPv is expected to increase the MORB's κ_{lat} by ~40% [42].

IV. CONCLUSIONS

In summary, we investigate the lattice thermal conductivity of cubic CaPv under the LM conditions utilizing the *ab initio* phonon quasiparticle approach and the pulsed light heating thermoreflectance measurement in a laser-heated DAC. Both the computational and the experimental techniques are able to deal with the cubic CaPv at high *P*-*T*, which is unquenchable at ambient conditions. CaPv's κ_{lat} is shown to vary with temperature as $1/T^{1.11}$, and to vary linearly with pressure. Throughout the LM, CaPv's κ_{lat} is roughly 2.5 times as large as that of MgPv. Being a strongly anharmonic material, CaPv's surprisingly large κ_{lat} is found to be mainly caused by the high crystal structure symmetry and the corresponding generally high phonon group velocities of the cubic primitive cell. Thermal conductivity of the pyrolitic mantle comprising of CaPv, bridgmanite, and ferropericlase is then modeled along the typical geotherm. Despite its relatively low abundance (7 vol%) in the pyrolite, CaPv increases the mantle's κ by ~10%, if accounted for. In mantle regions enriched in subducted crust, where CaPv is much more abundant (>23 vol% [61]), the κ will be more greatly enhanced.

ACKNOWLEDGMENTS

This work was funded primarily by the US Department of Energy Grant DE-SC0019759 (Z.Z. and R.M.W.) and in part by the National Science Foundation (NSF) grant EAR-1918126 (R.M.W.). This work used the Extreme Science and Engineering Discovery Environment (XSEDE), USA, which was supported by the NSF Grant ACI-1548562. Computations were performed on Stampede2, the flagship supercomputer at the Texas Advanced Computing Center (TACC), The University of Texas at Austin, generously funded by the NSF through Grant ACI-1134872. XRD measurements were performed at BL10XU, SPring-8 (Proposal No. 2019A0072, and 2019B0072) with help from Y. Ohishi. D.-B.Z. was supported by the Fundamental Research Funds for the Central Universities. K. Ohta was supported by the JSPS KAKENHI Grant 19H01995. K.H. was supported by the JSPS Grant 16H06285.

APPENDIX

1. Synthesis of $CaSiO_3$ Perovskite

We used pure natural wollastonite ($CaSiO_3$) powder as a starting material (Fig. S6(a) of the Supplemental Material [42]). We confirmed no aluminum was included in the wollastonite sample by energy dispersive spectroscopy analysis. The powder was shaped into a disk, and then we sputtered gold or platinum onto both sides of the sample disk, which played as both a laser absorber and a monitor for temperature rise in thermal conductivity measurements. High pressure was generated in a symmetric-type DAC using a pair of diamond anvils with 300 μm culet and a rhenium gasket that was pre-indented to a thickness of about 50 μm. We loaded the disk-shaped sample together with a single crystal sapphire plate (initial thickness: 30 μm) and NaCl pressure medium into a sample chamber with about 100 μm diameter drilled at the center of the gasket. The pressure was determined from the Raman spectrum of the diamond anvil at room temperature [82].

To synthesize $CaSiO_3$ perovskite (CaPv), we compressed the starting material to ~50 GPa at 300 K and then heated it to more than 1500 K from both sides using a pair of continuous wave fiber lasers for at least 60 mins. We collected thermal radiation from the sample and analyzed it in wavelengths between 550 and 750 nm to convert it into temperature in accordance with Planck's black body radiation law. The synthesis of CaPv was confirmed by utilizing synchrotron XRD experiments at the beamline BL10XU of SPring-8 (see sharp peaks from CaPv in Fig. S6(b) of the Supplemental Material [42]) [11,83]. Subsequently, we performed thermal diffusivity

measurements with changing pressure and temperature conditions. We performed thermal annealing every time after the pressure was adjusted to release deviatoric stress on the sample.

2. Experimental Determination of the High *P-T* κ_{lat} of CaPv

We performed three separate measurement runs up to 67 GPa and 1950 K (TABLE I). κ_{lat} is written with thermal diffusivity *D*, density ρ, and isobaric heat capacity C_P,

$$\kappa_{lat} = D\rho C_P. \quad \text{(A1)}$$

We obtained CaPv's ρ from its high-temperature equation of state [75] and C_P from thermodynamic relations and reported thermoelastic parameters of CaPv [12,78]. *D* was measured *in-situ* at high *P-T* by employing a combination of pulsed light heating thermoreflectance and laser-heated DAC techniques. A pulsed laser beam (thermoreflectance pump laser with 1064 nm wavelength, 1 ns pulse width, and 50 kHz frequency) irradiated the synthesized CaPv covered by a metal film to induce a temperature gradient within a few kelvins inside the sample. To observe the temperature change at the opposite side of the sample due to the pulse, we irradiated the opposite face of the sample with a continuous wave probe laser (thermoreflectance probe laser with 532 nm wavelength) to detect reflectivity changes due to the temperature change in the sample. During the operation of the thermoreflectance measurement, high-power continuous wave infrared laser beams (1064 nm wavelength) irradiated both surfaces of the sample to maintain a steady-state high temperature. The steady-state high temperatures were determined from the thermal radiation spectrum between 640 and 740 nm to fit Planck's law. The reliability of the high *P-T* thermoreflectance technique has been tested by comparing the measured thermal diffusivity of Pt and Fe up to 2000 K and 60 GPa with previous works that used different experimental approaches [24].

The obtained thermoreflectance signal of CaPv at 44 GPa and 1260 K is shown in Fig. S7(a) of the Supplemental Material [42]. Such transient temperature curves were fitted by the one-dimensional thermal conduction equation to estimate the heat diffusion time (τ) through the metal-CaPv-metal layers,

$$T(t) = \bar{T}\sqrt{\frac{\tau}{\pi t}}\sum_{n=0}^{\infty}\gamma^{2n}\exp\left[-\frac{(2n+1)^2}{4}\frac{\tau}{t}\right], \quad \text{(A2)}$$

where $T(t)$ is temperature as a function of time (t), $\bar{T}$ is a constant, and γ is a fitting parameter describing heat effusion to the pressure medium. The fitting yielded the τ within a 5% error. The

thicknesses of the recovered sample and metal layers were measured after the thermoreflectance measurements. We obtained a cross-section of the heated portion for CaPv synthesis by using a focused ion beam apparatus (Fig. S7(b) of the Supplemental Material [42]). Subsequently, thicknesses of the sample and metal layers were observed with a scanning electron microscope. Those thicknesses at high *P-T* conditions were estimated after the correction of elastic lattice expansion [84,85] and the pressure-induced amorphization of CaPv [86]. The error of the CaPv thickness was estimated from the standard deviation of the estimated thickness in the heated portion. We considered a three-layer heat diffusion model, namely heat diffusion through the sputtered metal layers, and extracted the thermal diffusivity of CaPv (D_{CaPv}) from the following equations,

$$D_{\mathrm{CaPv}} = \frac{\frac{\Gamma}{6}+1+\frac{1}{\Gamma}}{(\Gamma+2)\frac{\tau}{6}-(\Gamma+\frac{4}{3})\frac{d_{\mathrm{metal}}^2}{D_{\mathrm{metal}}}} d_{\mathrm{CaPv}}^2, \tag{A3}$$

$$\Gamma = \frac{C_{\mathrm{CaPv}} d_{\mathrm{CaPv}}}{C_{\mathrm{metal}} d_{\mathrm{metal}}}, \tag{A4}$$

where D_{metal} is the thermal diffusivity of metal (gold or platinum), d_{CaPv} and d_{metal} are the thickness of CaPv and metal, respectively, and C_{CaPv} and C_{metal} are heat capacity per unit volume ($C = \rho C_P$) of CaPv and metal, respectively. D_{metal} [87,88] and C_{metal} [84] of Au were estimated as previously reported [25]. Since the thickness of Au film (< 0.4 μm) was less than a tenth of the thickness of the CaPv sample (Fig. S7(b) of the Supplemental Material [42]), the uncertainties in the thickness and the thermophysical properties of metal (Au and Pt) does not affect the value of the obtained D_{CaPv}, which has been shown in our previous study for (Mg,Fe)SiO_3 postperovskite (see Experimental methods and S3 of the Supporting information of Ref. [25]).

The temperature uncertainty during high *P-T* thermoreflectance measurement, u_T, was estimated from the following,

$$u_T = \sqrt{u_{fit}^2 + u_{str}^2}, \tag{A5}$$

where u_{fit} and u_{str} are temperature uncertainties from Planck fitting error (Fig. S7(c) of the Supplemental Material [42]) and from temperature structure (heterogeneity) in the sample estimated using the finite element method simulation (see Ref. [24] for more details), respectively. The combined standard uncertainty in the obtained temperature during high *P-T* thermoreflectance measurement was estimated as 10%. Thermal pressures in the present high *P-T* experiments were estimated empirically based on earlier laser-heated DAC measurements for CaPv [89]. Further

details of the measurement system and the analytical methods of this approach can be found in our previous reports [24,25,90,91].

REFERENCES

[1] T. Lay, J. Hernlund, and B. A. Buffett, Nat. Geosci. **1**, 25 (2008).

[2] A. M. Hofmeister, Science **283**, 1699 (1999).

[3] A. Zerr, X. Diegeler, and R. Boehler, Science **281**, 243 (1998).

[4] R. M. Wentzcovitch, B. B. Karki, M. Cococcioni, and S. d. Gironcoli, Phys. Rev. Lett. **92**, 018501 (2004).

[5] A. F. Goncharov, P. Beck, V. V. Struzhkin, B. D. Haugen, and S. D. Jacobsen, Phys. Earth Planet. Inter. **174**, 24 (2009).

[6] K. Ohta, T. Yagi, N. Taketoshi, K. Hirose, T. Komabayashi, T. Baba, Y. Ohishi, and J. Hernlund, Earth Planet. Sci. Lett. **349–350**, 109 (2012).

[7] J. J. Valencia-Cardona, G. Shukla, Z. Wu, C. Houser, D. A. Yuen, and R. M. Wentzcovitch, Geophys. Res. Lett. **44**, 4863 (2017).

[8] W. F. McDonough and S.-S. Sun, Chem. Geol. **120**, 223 (1995).

[9] T. Sun, D.-B. Zhang, and R. M. Wentzcovitch, Phys. Rev. B **89**, 094109 (2014).

[10] D.-B. Zhang, T. Sun, and R. M. Wentzcovitch, Phys. Rev. Lett. **112**, 058501 (2014).

[11] T. Komabayashi, K. Hirose, N. Sata, Y. Ohishi, and L. S. Dubrovinsky, Earth Planet. Sci. Lett. **260**, 564 (2007).

[12] M. Noguchi, T. Komabayashi, K. Hirose, and Y. Ohishi, Phys. Chem. Miner. **40**, 81 (2013).

[13] A. R. Thomson, W. A. Crichton, J. P. Brodholt, I. G. Wood, N. C. Siersch, J. M. R. Muir, D. P. Dobson, and S. A. Hunt, Nature **572**, 643 (2019).

[14] R. Caracas, R. M. Wentzcovitch, G. D. Price, and J. Brodholt, Geophys. Res. Lett. **32**, L06306 (2005).

[15] X. Tang and J. Dong, Proc. Natl. Acad. Sci. U.S.A. **107**, 4539 (2010).

[16] P. Giura, L. Paulatto, F. He, R. P. S. M. Lobo, A. Bosak, E. Calandrini, L. Paolasini, and D. Antonangeli, Phys. Rev. B **99**, 220304(R) (2019).

[17] Y. Song, K. He, J. Sun, C. Ma, M. Wan, Q. Wang, and Q. Chen, Sci. Rep. **9**, 4172 (2019).

[18] H. Dekura, T. Tsuchiya, and J. Tsuchiya, Phys. Rev. Lett. **110**, 025904 (2013).

[19] X. Tang, M. C. Ntam, J. Dong, E. S. G. Rainey, and A. Kavner, Geophys. Res. Lett. **41**, 2746 (2014).

[20] N. Ghaderi, D.-B. Zhang, H. Zhang, J. Xian, R. M. Wentzcovitch, and T. Sun, Sci. Rep. **7**, 5417 (2017).

[21] H. Dekura and T. Tsuchiya, Geophys. Res. Lett. **46**, 12919 (2019).

[22] L. Stixrude, R. E. Cohen, R. Yu, and H. Krakauer, Am. Mineral. **81**, 1293 (1996).

[23] T. Sun, X. Shen, and P. B. Allen, Phys. Rev. B **82**, 224304 (2010).

[24] A. Hasegawa, T. Yagi, and K. Ohta, Rev. Sci. Instrum. **90**, 074901 (2019).

[25] Y. Okuda, K. Ohta, A. Hasegawa, T. Yagi, K. Hirose, S. I. Kawaguchi, and Y. Ohishi, Earth Planet. Sci. Lett. **547**, 116466 (2020).

[26] J. M. Ziman, *Electrons and Phonons: The Theory of Transport Phenomena in Solids.* (Oxford Univ. Press, Oxford, 2001).

[27] T. Sun and P. B. Allen, Phys. Rev. B **82**, 224305 (2010).

[28] G. Kresse and J. Furthmüller, Phys. Rev. B **54**, 11169 (1996).

[29] P. Giannozzi, S. Baroni, N. Bonini, M. Calandra, R. Car, C. Cavazzoni, D. Ceresoli, G. L Chiarotti, M. Cococcioni, I. Dabo, A. D. Corso, S. de Gironcoli, S. Fabris, G. Fratesi, R. Gebauer, U. Gerstmann, C. Gougoussis, A. Kokalj, M. Lazzeri, L. Martin-Samos, N. Marzari, F. Mauri, R. Mazzarello, S. Paolini, A. Pasquarello, L. Paulatto, C. Sbraccia, S. Scandolo, G. Sclauzero, A. P Seitsonen, A. Smogunov, P. Umari, and R. M Wentzcovitch, J. Phys.: Condens. Matter **21**, 395502 (2009).

[30] T. Tadano and S. Tsuneyuki, Phys. Rev. B **92**, 054301 (2015).

[31] N. K. Ravichandran and D. Broido, Phys. Rev. B **98**, 085205 (2018).

[32] C. Kwon, Y. Xia, F. Zhou, and B. Han, Phys. Rev. B **102**, 184309 (2020).

[33] Y. Xia, K. Pal, J. He, V. Ozoliņš, and C. Wolverton, Phys. Rev. Lett. **124**, 065901 (2020).

[34] O. Hellman and I. A. Abrikosov, Phys. Rev. B **88**, 144301 (2013).

[35] J. Klarbring, O. Hellman, I. A. Abrikosov, and S. I. Simak, Phys. Rev. Lett. **125**, 045701 (2020).

[36] Y. Lu, T. Sun, P. Zhang, P. Zhang, D.-B. Zhang, and R. M. Wentzcovitch, Phys. Rev. Lett. **118**, 145702 (2017).

[37] J.-W. Xian, J. Yan, H.-F. Liu, T. Sun, G.-M. Zhang, X.-Y. Gao, and H.-F. Song, Phys. Rev. B **99**, 064102 (2019).

[38] Y. Lu, T. Sun, and D.-B. Zhang, Phys. Rev. B **97**, 174304 (2018).

[39] Y. Lu, F. Zheng, Y. Yang, P. Zhang, and D.-B. Zhang, Phys. Rev. B **100**, 054304 (2019).

[40] Y. Lu, F. Zheng, Y. Yang, P. Zhang, and D.-B. Zhang, Phys. Rev. B **103**, 014304 (2021).

[41] Z. Zhang, D.-B. Zhang, T. Sun, and R. M. Wentzcovitch, Comput. Phys. Commun. **243**, 110 (2019).

[42] See Supplemental Material for details on the computational methodology and experimental measurements, which includes Refs. [43-67].

[43] D.-B. Zhang, P. B. Allen, T. Sun, and R. M. Wentzcovitch, Phys. Rev. B **96**, 100302(R) (2017).

[44] K. Esfarjani and G. Chen, Phys. Rev. B **84**, 085204 (2011).

[45] T. Luo, J. Garg, J. Shiomi, K. Esfarjani, and G. Chen, Europhys. Lett. **101**, 16001 (2013).

[46] J. Ma, W. Li, and X. Luo, Phys. Rev. B **90**, 035203 (2014).

[47] P. B. Allen, Phys. Rev. B **88**, 144302 (2013).

[48] G. M. Manthilake, N. de Koker, D. J. Frost, and C. A. McCammon, Proc. Natl. Acad. Sci. U.S.A. **108**, 17901 (2011).

[49] V. Haigis, M. Salanne, and S. Jahn, Earth Planet. Sci. Lett. **355–356**, 102 (2012).

[50] S. Stackhouse, L. Stixrude, and B. B. Karki, Earth Planet. Sci. Lett. **427**, 11 (2015).

[51] N. de Koker, Earth Planet. Sci. Lett. **292**, 392 (2010).

[52] W.-P. Hsieh, F. Deschamps, T. Okuchi, and J.-F. Lin, Proc. Natl. Acad. Sci. U.S.A. **115**, 4099 (2018).

[53] S. S. Lobanov, N. Holtgrewe, G. Ito, J. Badro, H. Piet, F. Nabiei, J.-F. Lin, L. Bayarjargal, R. Wirth, A. Schreiber, and A. F. Goncharov, Earth Planet. Sci. Lett. **537**, 116176 (2020).

[54] S. Stackhouse, L. Stixrude, and B. B. Karki, Phys. Rev. Lett. **104**, 208501 (2010).

[55] W.-P. Hsieh, F. Deschamps, T. Okuchi, and J.-F. Lin, J. Geophys. Res. Solid Earth **122**, 4900 (2017).

[56] D. A. Dalton, W.-P. Hsieh, G. T. Hohensee, D. G. Cahill, and A. F. Goncharov, Sci. Rep. **3**, 2400 (2013).

[57] N. de Koker, Phys. Rev. Lett. **103**, 125902 (2009).

[58] C. Carbogno, R. Ramprasad, and M. Scheffler, Phys. Rev. Lett. **118**, 175901 (2017).

[59] M. W. Ammann, A. M. Walker, S. Stackhouse, J. Wookey, A. M. Forte, J. P. Brodholt, and D. P. Dobson, Earth Planet. Sci. Lett. **390** (2014).

[60] F. D. Stacey and P. M. Davis, *Physics of the Earth.* (Cambridge Univ. Press, Cambridge, 2008).

[61] K. Hirose, N. Takafuji, N. Sata, and Y. Ohishi, Earth Planet. Sci. Lett. **237**, 239 (2005).

[62] H. Aramberri, R. Rurali, and J. Íñiguez, Phys. Rev. B **96**, 195201 (2017).

[63] A. M. Hofmeister, Phys. Earth Planet. Inter. **170**, 201 (2008).

[64] A. M. Hofmeister, Phys. Chem. Miner. **41**, 361 (2014).

[65] A. M. Hofmeister, Am. Mineral. **86**, 1188 (2001).

[66] J. P. Watt, G. F. Davies, and R. J. O'Connell, Rev. Geophys. **14**, 541 (1976).

[67] S.-H. Shim, R. Jeanloz, and T. S. Duffy, Geophys. Res. Lett. **29**, 19 (2002).

[68] P. E. Blöchl, Phys. Rev. B **50**, 17953 (1994).

[69] W. G. Hoover, Phys. Rev. A **31**, 1695 (1985).

[70] S. Baroni, S. d. Gironcoli, A. D. Corso, and P. Giannozzi, Rev. Mod. Phys. **73**, 515 (2001).

[71] P. G. Klemens, Proc. R. Soc. Lond. A **208**, 108 (1951).

[72] C. Herring, Phys. Rev. **95**, 954 (1954).

[73] S. Imada, K. Ohta, T. Yagi, K. Hirose, H. Yoshida, and H. Nagahara, Geophys. Res. Lett. **41**, 4542 (2014).

[74] T. Feng, L. Lindsay, and X. Ruan, Phys. Rev. B **96**, 161201(R) (2017).

[75] Z. Zhang and R. M. Wentzcovitch, Phys. Rev. B **103**, 104108 (2021).

[76] K. Kunc and K. Syassen, Phys. Rev. B **81**, 134102 (2010).

[77] M. L. Marcondes and R. M. Wentzcovitch, J. Appl. Phys. **117**, 215902 (2015).

[78] S. Gréaux, T. Irifune, Y. Higo, Y. Tange, T. Arimoto, Z. Liu, and A. Yamada, Nature **565**, 218 (2019).

[79] L. Lindsay, D. A. Broido, J. Carrete, N. Mingo, and T. L. Reinecke, Phys. Rev. B **91**, 121202(R) (2015).

[80] M. Simoncelli, N. Marzari, and F. Mauri, Nat. Phys. **15**, 809 (2019).

[81] L. Isaeva, G. Barbalinardo, D. Donadio, and S. Baroni, Nat. Commun. **10**, 3853 (2019).

[82] Y. Akahama and H. Kawamura, J. Appl. Phys. **100**, 043516 (2006).

[83] N. Sun, Z. Mao, S. Yan, X. Wu, V. B. Prakapenka, and J.-F. Lin, J. Geophys. Res. Solid Earth **121**, 4876 (2016).

[84] T. Tsuchiya, J. Geophys. Res. **108**, 1 (2003).

[85] M. Matsui, E. Ito, T. Katsura, D. Yamazaki, T. Yoshino, A. Yokoyama, and K. Funakoshi, J. Appl. Phys. **105**, 013505 (2009).

[86] K. Shimoda, H. Miyamoto, M. Kikuchi, K. Kusaba, and M. Okuno, Chem. Geol. **222**, 83 (2005).

[87] C. Y. Ho, R. W. Powell, and P. E. Liley, J. Phys. Chem. Ref. Data **1**, 279 (1972).

[88] R. G. Ross, P. Andersson, B. Sundqvist, and G. Bäckström, Rep. Prog. Phys. **47**, 1347 (1984).

[89] T. Kurashina, K. Hirose, S. Ono, N. Sata, and Y. Ohishi, Phys. Earth Planet. Inter. **145**, 67 (2004).

[90] T. Yagi, K. Ohta, K. Kobayashi, N. Taketoshi, K. Hirose, and T. Baba, Meas. Sci. Technol. **22**, 024011 (2011).

[91] K. Ohta, T. Yagi, K. Hirose, and Y. Ohishi, Earth Planet. Sci. Lett. **465**, 29 (2017).

TABLE I. Experimental pressures (P), temperatures (T), thermal diffusivities (D), and lattice thermal conductivities (κ_{lat}) of CaPv.

Run	P (GPa)	T (K)	D (mm^2/s)	κ_{lat} (W/m/K)
1	44(2)	1250(120)	3.49(53)	20.0(31)
	44(2)	1260(130)	3.14(46)	18.1(27)
2	52(2)	1330(130)	3.82(59)	22.2(34)
	52(2)	1370(140)	3.52(55)	20.6(32)
3	55(3)	300(0)	16.70(247)	37.3(55)
	67(3)	1950(200)	2.84(47)	18.3(30)

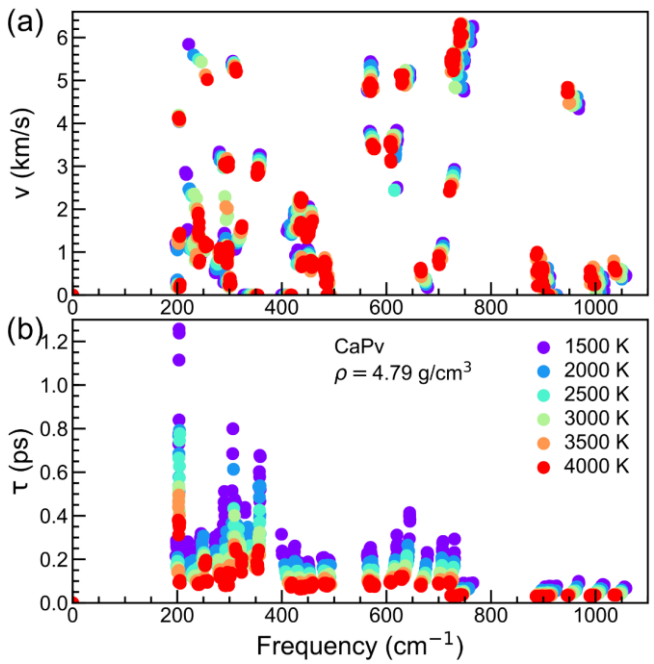

FIG. 1. (a) Phonon group velocities ($v_{\mathbf{q}s}$) and (b) lifetimes ($\tau_{\mathbf{q}s}$) of CaPv's phonon quasiparticles sampled by MD simulations using a $3 \times 3 \times 3$ supercell (135 atoms) vs. renormalized phonon frequency ($\tilde{\omega}_{\mathbf{q}s}$) at several temperatures.

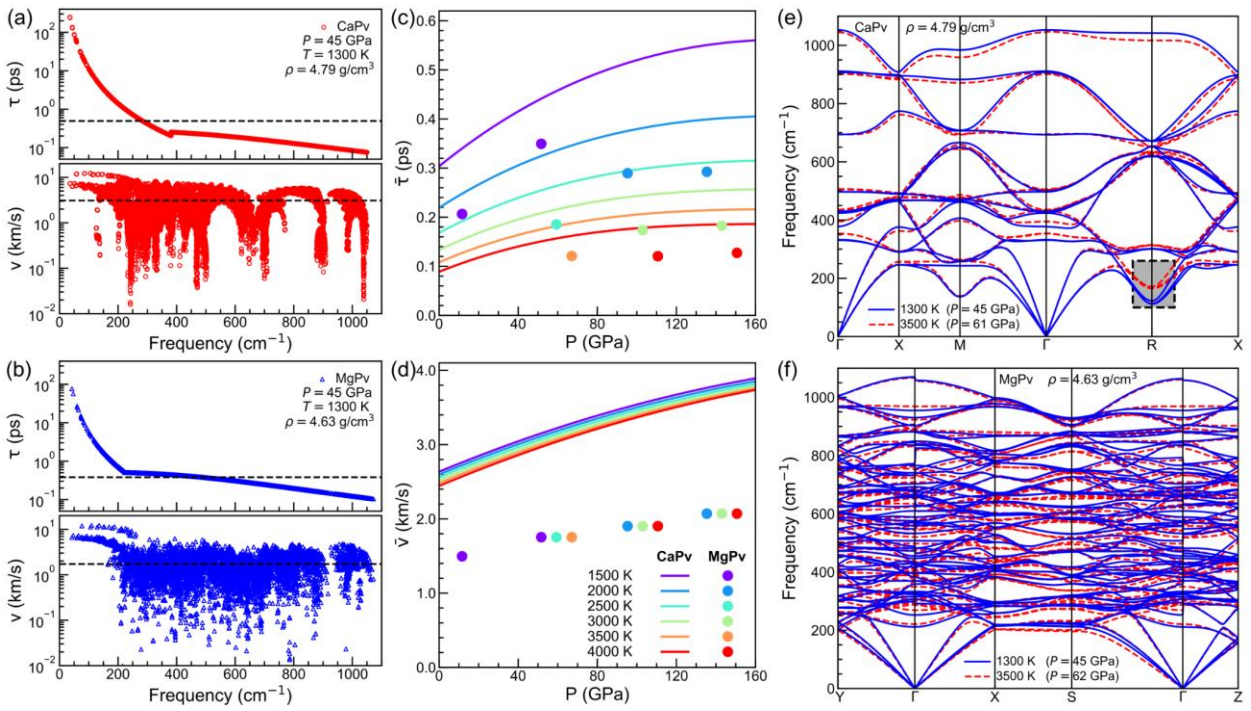

FIG. 2. (a) $\tau_{\mathbf{q}s}$ and $v_{\mathbf{q}s}$ sampled by a 20 × 20 × 20 q-mesh versus $\widetilde{\omega}_{\mathbf{q}s}$ of CaPv at T = 1300 K and ρ = 4.79 g/cm^3, corresponding to P = 45 GPa. (b) $\tau_{\mathbf{q}s}$ and $v_{\mathbf{q}s}$ sampled by an 8 × 8 × 8 **q**-mesh versus $\widetilde{\omega}_{\mathbf{q}s}$ of MgPv at the same P-T conditions and ρ = 4.63 g/cm^3. Dashed lines indicate average phonon lifetimes ($\bar{\tau}$) and average phonon velocities ($\bar{v}$). (c) $\bar{\tau}$ and (d) $\bar{v}$ of CaPv (solid curves) and MgPv (dots) versus P at various temperatures. (e) Anharmonic phonon dispersions at 1300 K (solid blue curves) and 3500 K (dashed red curves) at ρ = 4.79 g/cm^3 of CaPv, corresponding to P = 45 and 61 GPa, respectively. The dashed rectangle marks the phonon branches that are strongly temperature-dependent. (f) Anharmonic phonon dispersions at 1300 K (solid blue curves) and 3500 K (dashed red curves) at ρ = 4.63 g/cm^3 of MgPv, corresponding to P = 45 and 62 GPa, respectively.

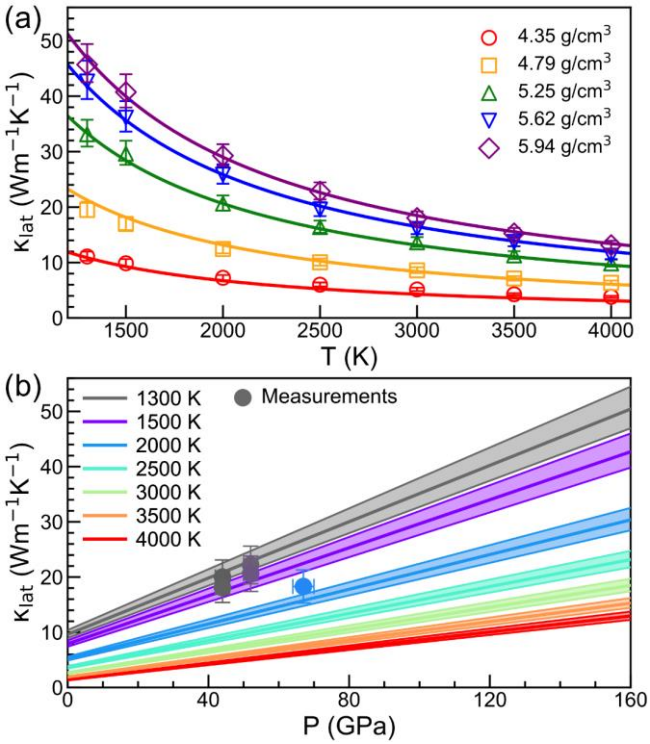

FIG. 3. (a) Lattice thermal conductivity (κ_{lat}) vs. *T* of CaPv (symbols) at several densities. Error bars show the computational uncertainties (6–7%) caused by fitting the frequency dependence of phonon quasiparticle linewidth [42]. The uncertainty arising from MD simulations is found to have negligible effects on the fitting and thus, in the final result for κ_{lat} (see test reported in Fig. S5 of the Supplemental Material [42]). Solid curves show the fitting to Eq. (4). (b) κ_{lat} versus *P* of CaPv at a series of temperatures. Shaded areas indicate the same computational uncertainties as in (a). Solid symbols with error bars are experimental measurements.

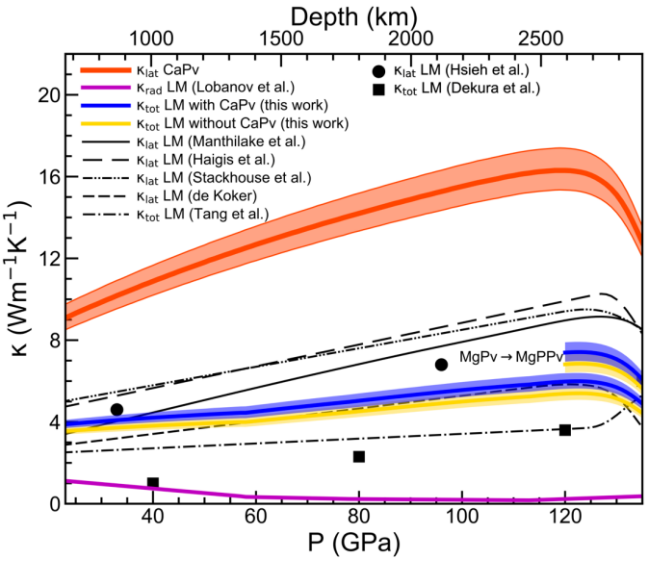

FIG. 4. Thermal conductivities along the geotherm [60]. κ_{lat} of CaPv is shown in orange, the experimental radiative thermal conductivity (κ_{rad}) [53] of a pyrolitic aggregate is shown in purple, the total thermal conductivity (κ_{tot}) of the LM without CaPv is shown in yellow and with CaPv in blue. Shaded areas indicate computational uncertainties. Available estimations of κ_{lat} [48-52] and κ_{tot} [18,19] of the LM are shown for comparison.